Effects of Postpulse Surface Temperature on Micropulsed Plasma Thruster Operation

Erik L. Antonsen* and Rodney L. Burton†
University of Illinois at Urbana–Champaign, Urbana, Illinois 61801
Garrett A. Reed‡
W.E. Research, Rosamond, California 93560
and
Gregory G. Spanjers§
U.S. Air Force Research Laboratory, Kirtland Air Force Base, New Mexico 87117

High-speed mercury cadmium telluride photovoltaic detectors sensitive to infrared emission are used in a micropulsed plasma thruster (micro-PPT) to explore the surface-temperature profile throughout the discharge process for an ablative arc over Teflon™. Real-time surface-temperature measurements are made after the current pulse ends in a micro-PPT to examine heating methods and ablation characteristics of the Teflon® propellant. Calibration is performed on heated Teflon, experimentally accounting for temperature-dependent variations in emissivity. Time-dependent measurements are taken of the fuel face and used to determine a surface-temperature profile after the arc. Photographs of the arc breakdown are taken with a gated, intensified camera capable of 5-ns shutter times allowing visual interpretation of the arc emission in terms of nonaxisymmetric arc spoking effects. The data are analyzed to calculate Teflon vapor pressure and expected impulse bit contribution of the neutral vapor liberated from the fuel face during the ablative cooling process. The cooling profile is also compared with predictions from a code that is under development. Finally, methods for using this sensing technique during the current pulse of the thruster are proposed and evaluated for future applications.

Nomenclature

A	=	detector active area, mm^2
a	=	gas sound speed
a_4	=	sound speed where gas is at rest
D^*	=	normalized photovoltaic detectivity
F	=	molecular flux
G	=	amplifier gain (V/A)
I	=	thruster current, A
k	=	Boltzmann constant
k_o	=	optical constant
L'	=	inductance gradient
m	=	molecular weight
n_n	=	neutral vapor density
P_E	=	spectral emissive power, W/m^2 μm
p_c	=	characteristic pressure
p_{eq}	=	equilibrium vapor pressure
R	=	specific gas constant
R_p	=	peak detector responsivity (A/W)
r_i	=	central electrode radius
r_o	=	outer electrode radius
T	=	temperature, K
T_c	=	characteristic temperature
T_s	=	surface temperature, K
t	=	time
u	=	gas velocity
$\bar{u}$	=	average gas velocity
V	=	voltage
x	=	axial distance from propellant face
γ	=	ratio of specific heats
ε_λ	=	wavelength dependent emissivity of Teflon®
λ_{mfp}	=	mean free path
μ_0	=	permeability of free space
ρ	=	gas density
$\rho 4$	=	gas density where gas is at rest
σ	=	molecule cross-sectional area
$\int T dt_{EM}$	=	electromagnetic impulse bit

Introduction

WITH the increasing presence of micropropulsion options for spacecraft attitude control and propulsion, there is a corresponding need for the development of experimental techniques to understand the operating physics of these devices better. A class of micropulsed plasma thrusters (micro-PPTs)[1] is being developed to address these needs. These devices use Teflon™ propellant to provide precise impulse bits in the 10-μN-s range. In the near term, these thrusters can provide propulsive attitude control on 150-kg class spacecraft at 1/10 the dry mass of conventional torque rods and reaction wheels.[1]

However, the micro-PPT still suffers the same deficiencies that standard PPTs have been dealing with since their inception. Low mass utilization coupled with spacecraft contamination concerns provide a continuing emphasis for research to improve these systems. Ultimately, postpulse late-time ablation in these thrusters defines operation and performance capability by sustaining significant propellant mass loss per pulse that fails to contribute to thrust. This phenomenon is called late-time ablation (LTA) and has been estimated to account for 40–90% of the total mass loss from various sources.[2,3]

Significant research effort has been expended attempting to characterize LTA in terms of plume effects both from neutral vapor interferometric measurements[4] and analysis of macroparticle ejection.[2] Past experiments have demonstrated a correlation between propellant temperature and thruster operating efficiency. Spanjers et al. inserted thermocouples into the Teflon® propellant of parallel-plate PPTs to varying depths from the fuel face to measure steady-state operation temperatures at long times.[5] Of note from this study is an increased efficiency when the propellant is operated at lower average temperatures. Unfortunately, the thermocouple location behind the propellant surface exposed to the plasma can only provide the steady-state measurement of the bulk fuel temperature. The time resolution of these devices is limited by the metal junction size, and any attempt to place thermocouples directly on the propellant surface exposes the thermocouple joint to the arc discharge.

To obtain a time-resolved measurement of the surface temperature, mercury-cadmium-telluride (HgCdTe) photovoltaic detectors are used. These detectors exhibit the time resolution required to investigate the microsecond capacitive discharges in micro-PPTs. These detectors have found substantial use in the study of dynamic crack propagation, where they are used to evaluate conversion of work to heat at the tips of fast-moving cracks in solid materials.[6,7] Application of these detectors to the problem of an ablation-controlled arc has been the subject of recent research.[8] Their ability to measure postpulse surface temperatures on the micro-PPT has recently been validated.[8]

The infrared theory used to predict detector output has been detailed elsewhere, and so only a cursory treatment is given here. For calibration purposes, the HgCdTe detectors must view Teflon heated from room temperature to the maximum temperature measurable. For the purposes of this paper, the maximum temperature is about 750 K and is limited by Teflon deformation. Infrared radiation (TR) from the heated Teflon is defined by the Planck function and modified by a wavelength dependent emissivity. An estimate of the emissivity of Teflon is given in Ref. 8. Detector output voltage corresponding to heated Teflon is calculated by

$$V = k_o G A (1 - \cos\theta) \int_\lambda \varepsilon_\lambda D^* R_p P_e \, d\lambda \qquad (1)$$

where k_o is the transmissivity and reflectivities of any mirrors or windows in the optics system, G is the amplifier gain (20,000 V/A), θ is the half-angle of the solid angle viewed (radians), A is the detector active area (80×80 μm), P_E is the spectral emissive power (W/m^2μm) defined by the Planck function,[8] D^* is the normalized detectivity of the specific detector used, and R_p is the peak responsivity of the specific detector used (8.2 A/W).

For Teflon temperatures exceeding 750 K, this calculation is used to provide a calibration number for the detector voltage. When the detectors are applied to an operating micro-PPT, this calibration allows temperature determination for postpulse temperature measurements. During the pulse, the experimental setup used here is not optimal for measuring the Teflon temperature because of the presence of plasma emission and electronic noise. However, postpulse measurements allow for characterization of the contributions from LTA to mass loss and thrust. These measurements are compared with surface-temperature predictions made by the Keidar–Boyd model[9,10] for micro-PPT discharges to validate the model.

Experimental Apparatus

Detector

Experiments here are performed with a linear array of four 80×80 μm HgCdTe detector elements.[¶] The detectors are a p-n junction photodiode with preamplifier for each channel. For simplicity, only a single detector in the array of four is used. These detectors are housed in a liquid-nitrogen dewar to minimize thermal

noise from the substrate and support structure. A bias is applied to each detector of −5 mV.

Optics

The detector optics use a Newtonian telescope that images the surface of the fuel at 1:1 magnification over the detectors. The mirrors in the telescope are gold plated for 99% reflectivity in long-wave IR. A spherical mirror with a 304.8-mm focal length and a 50.8-mm-diam flat mirror create the telescope. The detectors are kept at vacuum behind a zinc-selenide (ZnSe) window with a 60-deg cone of view. A 25.4-mm-diam ZnSe window provides optical access into the vacuum chamber for thruster operation and calibration tests. During calibration, background thermal fluctuations are kept to a minimum by encasing the detector and telescope in a cardboard enclosure that has aluminum foil attached to the outside to reflect infrared radiation away from the setup.

Calibration

The calibration setup uses a 3.175-mm sheet of Teflon sandwiched between two copper plates with optical access holes 5.38 mm in diameter in both plates. The Newtonian telescope images the detectors at 1:1 magnification onto the Teflon surface. Only the front plate is heated so that there is no heat source behind the hole. Figure 1 shows a schematic of this setup.

Not shown in Fig. 1 is the additional zinc selenide vacuum chamber window (25.4 mm diam) that limits the solid angle of observable emission. A typical calibration takes about 10 h because a slow heating scheme is used to increase accuracy by reducing transient thermal effects. Three type K thermocouples are drilled into the sides of the Teflon sheet and embedded close to the point where the IR detector is imaged. Because of Teflon deformation at elevated temperatures, an upper temperature limit of 750 K is experienced for calibrations using this technique.

Temperature Measurements on Thrusters

For these tests, a two-electrode micro-PPT with 2.98-μF capacitor is used. Measurements of the surface are taken using the Newtonian telescope to image the surface onto the detectors. Targeting is performed via two 0.08-mm-diam tungsten wires crossed vertically and horizontally. This cross is imaged onto the detector for rough adjustment onto the detector. For fine adjustment, current (1.2 A) is run through each wire, and the thermal signature is detected and maximized by adjusting the optics slightly.

The thruster configuration is a two-electrode test bed with a 6.35 mm outer diameter and with the propellant flush with the exit plane. A capacitive discharge typical of an resistor-inductor-capacitor circuit generates the plasma at the exit plane of the thruster. The discharge energy is 4.35 J.
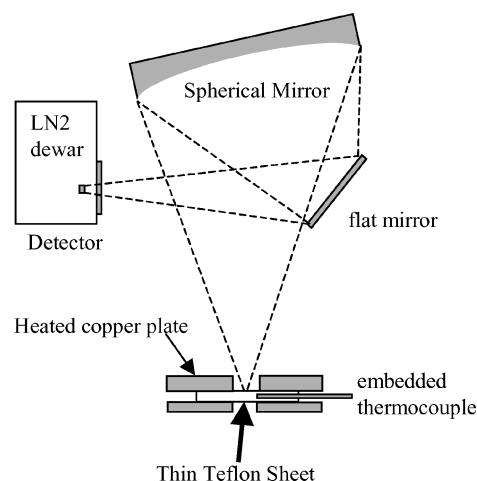
Fig. 1   **Teflon is sandwiched between a heated copper plate and a backplate. There is no heat source behind the optical access holes.**

The detector images are targeted on Teflon between the two electrodes. Because 1:1 imaging is used, the spatial resolution is the size of the detector area. Spatial resolution of the single detector used is 80×80 μm square on a micro-PPT diameter of 6.35 mm. Figure 2 shows the detector images to scale on the micro-PPT face. Because of arc spoking, the small coverage area used by the four-diode detector is not guaranteed to see the direct effects of the arc. Multiple pulses are taken to define an average and standard deviation surface temperature in real time.

Experimental Results

Calibration

Calibration for heated Teflon is performed using the apparatus shown in Fig. 1 and Eq. (1). There is a difference in emissivity between Teflon that has not been exposed to the plasma in a micro-PPT (virgin Teflon) and Teflon that has been exposed. Because the top layers of Teflon in the thruster undergo thermal cycling from repetitive pulsing, changes in the crystalline structure result in a slightly different emissivity than virgin Teflon. The full implications of this difference are discussed elsewhere,[8] but an important consequence is that the calibration curve differs if the Teflon has been preexposed to a plasma. Figure 3 shows the experimental calibration curves for virgin Teflon and plasma-exposed Teflon. For the latter experiments, the thruster face is conditioned with ~100 pulses before testing. The plasma-exposed calibration curve is used to translate detector voltages into the temperature domain.

Representative data points from experimental calibrations are shown along with a parabolic fit of those data points. These are also compared with a theoretical prediction from Eq. (1) (which lies almost directly on the parabolic fit). The fit for the plasma-exposed
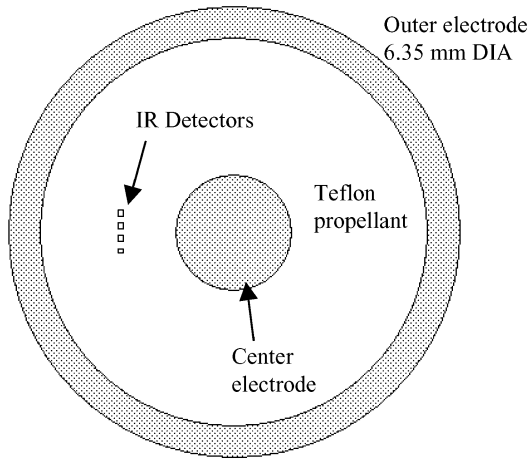
Fig. 2   Linear HgCdTe detectors shown on a micro-PPT face. The small □ are the detector images and the gray ○ are the micro-PPT electrodes. This drawing is to scale.
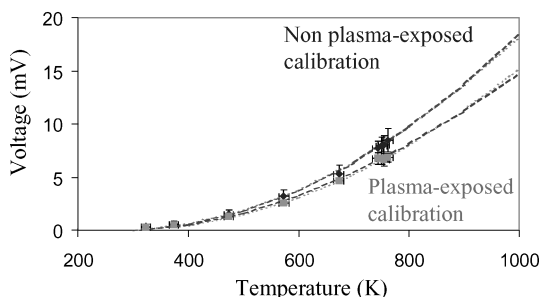
Fig. 3   Calibrations were performed with virgin Teflon and Teflon exposed to micro-PPT plasma conditions. The plasma-exposed data are used for calibration.

calibration curve is

$$V = 2.87 \times 10^{-5}\, T^2 \tag{2}$$

Beyond the peak measured temperature of 750 K, the voltage is calculated using Eq. (1).

The uncertainties in Fig. 3 are calculated by a rms standard deviation of five calibration tests combined with the $\pm$0.3-mV limitation of the detector. Also shown are temperature uncertainties using the same method based on the thermocouple uncertainty. For the K-type thermocouples used, the uncertainty is $\pm$2.2 K or 0.0075*T, whichever is larger. Another term is introduced for $\pm$8 K representing the temperature difference between the embedded thermocouple location and the center of the calibration target, where emission measurements are made. This value is obtained from experimental data and ANSYS computer code predictions shown in Ref. 8.

Pulse Imaging

Prediction of the surface temperature up to this point has generally assumed an azimuthally symmetric current sheet during the micro-PPT discharge. Intensified images of an operating micro-PPT at varying energies (Fig. 4) suggest that as the energy increases the arc attachment to the outer electrode can become localized by the onset of anode and/or cathode spots. Angular localization of the arc is a constriction of the current caused by increased magnetic field strength at high currents and minimization of arc resistance due to ohmic heating. This behavior has ramifications for both measurement and prediction of surface temperature.

When the current constricts, it is assumed to do so in a linear fashion between the electrodes. Although this might not be the case physically, for the purposes of calculations in the Keidar–Boyd model this assumption is necessary, and there is currently no evidence against this assumption. Within this constriction, the current density rises significantly, leading to an increase in ohmic heating of the plasma (proportional to the square of the current density). The result is an increase in heat flux to a localized area of propellant, which leads to locally high surface temperature and ablation rate. Because the surface temperature directly underneath the arc is dominated by particle convection, this area experiences the highest temperatures on the propellant face. Away from the arc, the heat transfer caused by particle convection is minimal, and the surface temperature is dominated by radiation from the arc, resulting in significantly reduced temperature predictions for this region. These temperature differences are significant because they provide an expected range of surface temperatures dependent on arc proximity.
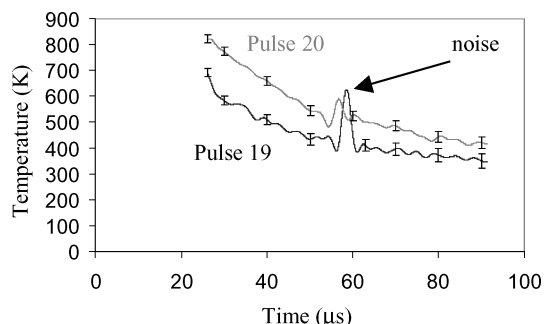
Postpulse Surface Temperature

Data taken during the pulse show interference from both plasma emission and electrical noise. To determine when data are measuring the surface and not the plasma, measurements are taken through the plasma sideways without looking at the thruster. Consistently, after the current pulse ends plasma emission contribution also ends,[8] allowing measurement of the postpulse surface emission. A zero-phase-shift Butterworth filter was applied to filter electrical noise. Figure 5 shows temperature results for 14 consecutive pulses. Because of plasma and electrical interference, data before 26 μs are considered invalid here. From 26 μs on, the data show experimental surface temperature measurements tracing the cooling of the propellant after the pulse. Each pulse shows noise at about 55 μs, which

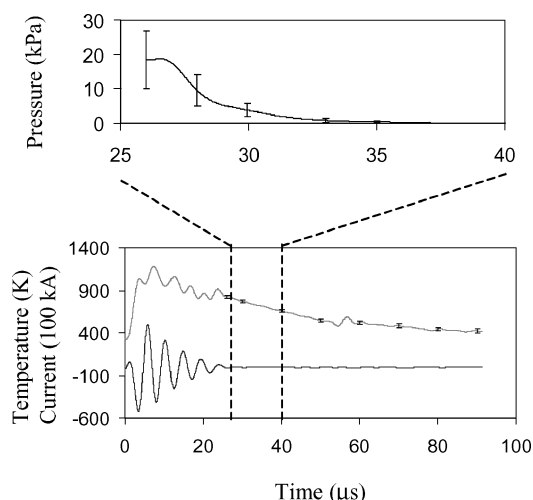Anode spots
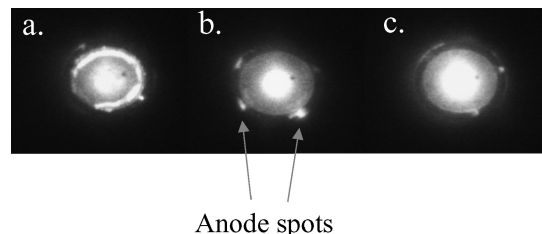
Fig. 4   Intensified images showing arc behavior at a) 2.3 J, b) 5.55 J, and c) 6.73 J. Capacitance is 0.417 μF.
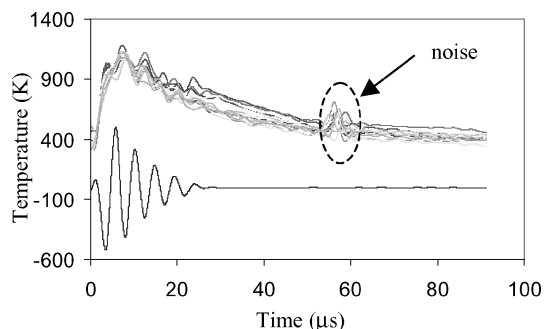
Fig. 5   Test with 14 pulses shows the spread of cooling temperatures measured. Valid data begin after the current pulse ends (26 μs).

Fig. 6   Postpulse temperature from two different micro-PPT firings.

Fig. 7   Surface temperature and thruster current for pulse 20. From 26–40 μs the Teflon vapor pressure is calculated. Data before 20 μs are not valid.

is traced to electromagnetic interference from the spark plug used to ignite the thruster. It is possible that the spread in experimental data reflects arc constriction effects. This is discussed more in the following.

Figure 6 shows the postpulse cooling curve for two distinct micro-PPT firings. A significant temperature difference is observed between the individual pulses, which is attributed to unpredictable changes in the surface-discharge arc location from pulse to pulse. Photographs of the thruster face indicate that spoking is common at typical firing energies for micro-PPTs.[11] The Teflon vapor pressure can be estimated from the propellant cooling curve data after the arc has extinguished.

Figure 7 shows the current discharge and surface temperature for pulse 20. Because of noise problems, the only acceptable data for the surface temperature calculation are after 20 μs. The 25–40-μs timeframe is expanded, and the pressure calculations shown are based on Turchi's[12] application of the Clausius–Clapeyron equation

to Wentink's experimentally measured neutral vapor pressure of Teflon.[13] Uncertainty is not calculated for the pressure data because uncertainty for Wentink's pressure measurements is not available. High sensitivity to the surface temperature is evident from the vapor pressure calculation immediately following 20 μs, where some of the electrical noise is factoring significantly into the calculation.

Thruster Performance

The natural vapor pressure of heated Teflon is given by Wentink.[13] The mathematical description of this curve is[12]

$$p_{eq} = p_c e^{-T_c/T_s} \qquad (3)$$

where $p_c = 1.84 \times 10^{15}$ N/m^2 and $T_c = 20{,}815$ K (Ref. 12). Combining this estimate of the vapor pressure with the measured surface temperature yields a time-dependent pressure calculation relevant to neutral vapor generation after the pulse. Because the pressure is logarithmically dependent on the surface temperature, small changes in temperature can result in large differences in pressure. The pressure uncertainty shown in Fig. 7 is based only on the uncertainty in the temperature measurement.

The pressure can be used to calculate the impulse bit gained from the postpulse neutral vapor generation. Assuming a symmetrical current sheet, the exposed Teflon propellant area is 2.13×10^{-5} m^2. Combined with the pressure, this gives an instantaneous force on the propellant face caused by the vapor pressure. Integrating this through the measurement time yields the impulse accumulated through the ablative cooling process (Fig. 8). The total calculated impulse bit from postpulse neutral generation is 1.1 ± 0.5 μN-s with the largest contribution occurring before 40 μs. Percentage of total impulse is discussed next.

The ideal-gas law can be used to calculate the total number of particles liberated per unit volume,

$$n_n = (p_c/kT_s)e^{-T_c/T_s} \qquad (4)$$

where k is the Boltzmann constant (1.38×10^{-23} J/K). Assuming that after the current pulse each particle liberated is a CF$_2$ monomer, the average particle mass is 50 atomic mass units. Multiplying this value by Avogadro's number gives an individual molecule mass of 8.3×10^{-23} g/particle. Using calculations for thermal evaporation common to particle vapor deposition,[14] the surface temperature and vapor pressure can be related to a molecular flux through

$$F = p_{eq}/\sqrt{2\pi mkT_s} \qquad (5)$$

This relationship is derived from the Clausius–Clapeyron equation. The molecular flux F is the number of molecules liberated from the surface per unit area per unit time. Using the data from pulse 20 and assuming that the surface temperature measured is representative of the total surface temperature, the molecular flux can be multiplied by the propellant surface area and integrated through time to yield a total molecular evaporation and therefore a total postpulse mass loss. Figure 9 shows the integration of the mass loss (and molecular evaporation) through time with typical uncertainties.
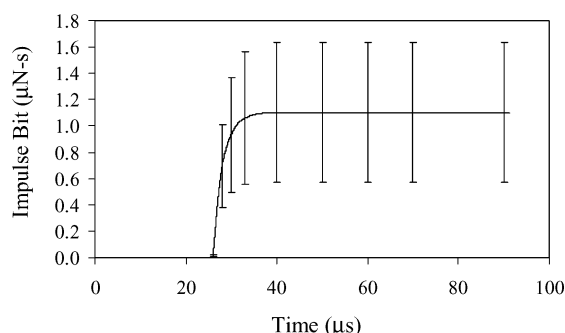
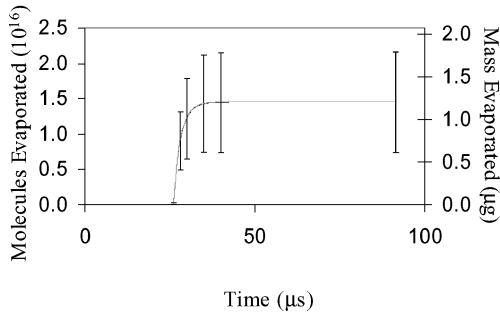**Fig. 8   Post-pulse impulse bit contribution from neutral vapor is calculated using the pressure shown in Fig. 7.**

Fig. 9 Total number of molecules and mass evaporated based on the surface temperature measurement of pulse 20.

The total mass lost through postpulse evaporation is $1.2 \pm 0.6 \ \mu g$. The average total mass lost per pulse (5.2 μg/pulse) is measured by pulsing 10,000 times and measuring thruster mass before and after the pulse. The postpulse mass loss as a percentage of the total mass lost is $23 \pm 11\%$. Note that the assumption of the measured surface temperature across the propellant face does not necessarily apply because of arc spoking. When the averaged temperature and uncertainties from pulse 19 are used, the mass loss drops to $0.0176 \pm 0.046 \ \mu g$. This suggests that in areas where the arc is not directly over the propellant face the expected amount of Teflon liberated from the surface is extremely low for a given pulse.

It is also useful to estimate an exhaust velocity for these neutral particles evaporated after the pulse. It is assumed that because there is no energy source after the pulse the surface temperature T_s is also the temperature of the evaporated gas just above the surface. Using the molecule mass from before, the specific gas constant R is calculated as 166 J/kg-K. Assuming that the Teflon vapor is a thermally and calorically perfect gas and that the gas temperature is the same as the Teflon surface, the speed of sound for that gas is $a = \sqrt{(\gamma R T)}$. Given the expected peak temperature of 750 K, the CF_2 molecule is assumed not to vibrate, and then has three translational and three rotational degrees of freedom. This gives CF_2 a ratio of specific heats of $\gamma = (6 + 2)/6$ or 1.33. Because this is a neutral gas, a billiard ball approximation for the cross section applies. The diameter of the CF_2 molecule is estimated to be ~ 3 Å, which results in a cross-sectional area σ of 7.07×10^{-20} m^2. Using the neutral density calculated from Eq. (4), a mean free path can be calculated from

$$\lambda_{\mathrm{mfp}} = 1/n_n \sigma \tag{6}$$

At the start of pulse 20, the mean free path is 8.7 μm. Taking the thruster diameter (0.00635 m) as a characteristic length, the Knudsen number is then about 10^{-3}, well within the collision-dominated regime. At about 40 μs the Knudsen number reaches 1, suggesting that a rarefied gas dynamic description might apply thereafter. However, because the neutral vapor is dense up to that point, a fluid-dynamic-centered expansion wave approximation is used to estimate the expected exhaust velocity.

We approximate the two-dimensional axisymmetric expansion of the postpulse ablated Teflon as one dimensional for the purpose of calculating the axial momentum and impulse bit. The justification is that the condition for one-dimensional expansion is a small axial vapor length compared to the source diameter. An estimate of the maximum axial length of the postpulse neutral vapor is m/ρA. Using Eq. (4), the neutral density ρ is 2.6×10^{-2} kg/m^3, and the exposed Teflon surface area A is 2.1×10^{-5} m^2, which give an axial length of ~ 2 mm or about $\frac{1}{3}$ of the thruster diameter. We make an assumption that pressure drives the flow in the axial direction and produces a small impulse bit caused by LTA. The measured half-angle of expansion for micro-PPTs is ~ 20 deg, which contributes a cosine loss of about 6%. Therefore, it is a reasonable approximation to use the method of characteristics as applied to unsteady flow by Anderson[15] to describe the gas expansion away from the propellant surface.

Along a characteristic, the value of

$$u + 2a/(\gamma - 1) = \text{const} \tag{7}$$

where u is the expanding gas velocity and a is the local speed of sound. Equation (7) can be modified to give a ratio of the local sound speed anywhere in the flow to the location, where the local wave velocity is equal to the sound speed (Mach number $= 1$). This is given by

$$a/a_4 = 1 - [(\gamma - 1)/2](u/a_4 - 1) \tag{8}$$

where a_4 denotes the location of unity Mach number. Taking the surface temperature as the gas temperature at the surface and averaging from 25 until 40 μs, an average gas temperature of 740 K is calculated. Using isentropic relations, the gas temperature at the point where $M = 1$ is calculated as 635 K, which translates to an a_4 value of 375 m/s. Equation (8) can be manipulated through the isentropic relations to give a density ratio of

$$\rho/\rho_4 = \{1 - [(\gamma - 1)/2](u/a_4 - 1)\}^{2/(\gamma - 1)} \tag{9}$$

A density-weighted average for the expansion wave velocity can be calculated by numerically integrating

$$\bar{u} = \frac{\int \rho u \, dx}{\int \rho \, dx} \tag{10}$$

where the integral of $\rho \, dx$ gives the total mass. The technique used to perform this integral is to use the following relation from Anderson, which is a property of the method of characteristics:

$$x = t\{u - a_4 + [(\gamma - 1)/2]u\} \tag{11}$$

The integrals in Eq. (10) can be transformed into velocity integrals by taking the derivative of Eq. (11), which gives

$$dx = t[(\gamma + 1)/2] \, du \tag{12}$$

When Eq. (12) is substituted into the two integrals in Eq. (10), the integral is performed from a_4 to $u_{\max}$. The time term is a constant in both integrals and therefore drops out. Because the background pressure is a vacuum, the density will decrease as the gas expands allowing an isentropic transition to supersonic velocities even after the current pulse has ended. Ultimately, the numerical solution to Eq. (10) is $\bar{u} = 1.75 a_4$. Using a_4 from the preceding, the average velocity from the centered expansion wave approximation is ~ 655 m/s, which yields an I_{sp} of ~ 60 s for the postpulse exhaust contribution. Combining this with the mass loss estimated from Eq. (5), a total impulse bit from the postpulse ablation can be calculated again. The impulse bit estimated from this technique is $0.8 \pm 0.4 \ \mu$N-s. This is within the uncertainty of the impulse bit calculated from the surface pressure of $1.1 \pm 0.5 \ \mu$N-s.

These impulse bit values can be compared with the calculated electromagnetic impulse bit. The electromagnetic impulse bit[16] is calculated by

$$\int T \, dt_{\mathrm{EM}} = \frac{1}{2} L' \int I^2 \, dt \tag{13}$$

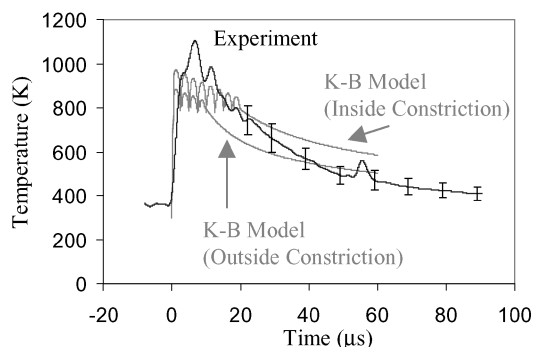where I is the current measured with the Rogowski probe and L' is defined by

$$L' = (\mu_o/2\pi)\left[\ell n(r_o/r_i) + \tfrac{3}{4}\right] \tag{14}$$

where μ_o is the permeability of free space $(4\pi \times 10^{-7}$ H/m) and r_o and r_i are the outer and inner electrode radii, respectively. Using the current pulse measured for pulse 20 yields an expected electromagnetic impulse bit of 19 μN-s. There is also an electrothermal (ET) impulse bit contributed during the pulse from neutral vapor. Without accurate thrust data for the 6.35-mm micro-PPT or surface temperature data during the pulse, the ET impulse bit is difficult to estimate, but it is likely to add significantly to the total impulse bit. Assuming no ET contribution, the late-time neutral vapor generated can contribute a maximum of 8% of the total thrust. This figure is probably a significant overprediction.

Theoretical Comparisons

The Keidar–Boyd (K-B) model predicts surface temperatures both near and far from a theoretical arc spoke location. "Near" refers to surface temperature from an area that was directly underneath the current constriction, and "Far" refers to a distant section of propellant face that receives only radiation from the spoke. These predictions provide the maximum and minimum temperatures expected during the cooling phase as well as an expected distribution of cooling curves based on proximity to the arc location. Figure 10 shows a comparison of both predictions to the average cooling temperature from the 14 pulses shown in Fig. 5. The expected cooling corridor from the prediction is close to the statistical spread of the experimental data. Of particular importance is immediately postpulse (26 μs) the experimental and predicted surface temperatures are close to the same range. The experimental cooling profile is similar to the predicted profile, but cools faster. The K-B model considers only ablation as the heat removal mechanism from the propellant face. By omitting radiation from the surface and thermal conduction into the surface, their prediction cools at a slower rate than is measured. The experimental data suggest that radiation and thermal conduction mechanisms should be included for a more accurate cooling curve prediction.

Keidar's specific predictions concerning surface temperature near and far from arc constriction can be evaluated by comparison with single pulses that mark the highest and lowest temperatures measured. It is thought that a temperature measurement made in a location directly under the constriction will have the highest temperature
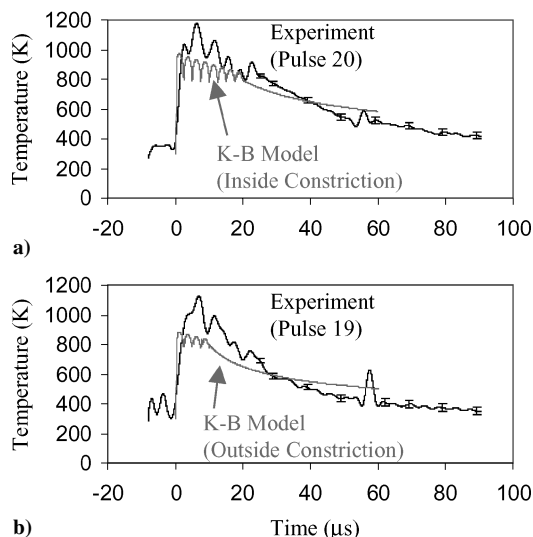
postpulse cooling curve and that one far from the constriction (i.e., heated only by radiation) will have the lowest temperature cooling curves observed. Any spread between these values can reflect changes in proximity to the actual constriction location. Figure 11 shows comparison of a) the highest temperature cooling curve from the data set (pulse 20) compared with the surface temperature predicted for an area covered by the arc constriction, and b) shows a comparison of the lowest temperature cooling curve from the data set (pulse 19) compared with the surface temperature predicted for an area far from the arc constriction. The difference in these measurements suggests that the arc was moving randomly around the propellant face during testing. This is not conclusive proof, as two-dimensional imaging of the propellant face in the long wavelength IR would be required to assess the constriction location positively on a pulse-to-pulse basis.

Conclusions

Postpulse surface temperature measurements allow calculation of a number of performance parameters describing late-time-ablation contributions. Because of arc spoking and spatial resolution limitations, there are unavoidable assumptions concerning application of the measured temperatures to the entire propellant face. The postpulse cooling curve allows calculation of postpulse performance for the micropulsed plasma thruster (micro-PPT). Using a pressure gradient calculation for the postpulse impulse bit, a value of 0.8 ± 0.4 μN-s is obtained. Using a centered expansion wave description, the postpulse impulse bit for a 4.35 J micro-PPT is 1.1 ± 0.5 μN-s. The postpulse neutral vapor mass loss is 1.2 ± 0.6 μg, which is $23 \pm 11\%$ of the 5.2 μg/pulse measured average mass loss. The assumptions required for these calculations suggest that they define the upper boundary of possible performance, in part because of the limited information on arc spoke dimensions and location. The specific impulse of the postpulse neutral vapor is calculated to be $\sim$60 s.

These data demonstrate that Keidar's theory predicts postpulse cooling temperatures well. Experimental curves show faster cooling, but beginning temperatures are within the same temperature range as the predictions. This model includes ablation as the only cooling mechanism and neglects thermal conduction into and across the propellant face as well as radiation from the propellant into space. Were these effects to be included, the predicted cooling rates would likely be closer to experimental measurements.

Fig. 10   Average of 14 pulses with standard deviation is compared to predictions from the K-B model both within and outside a theoretical arc spoke.

Fig. 11   Comparison of the predicted surface temperature a) within an arc constriction to pulse 20, which showed the highest temperature of the data set, and b) shows the prediction far from the arc constriction location with pulse 19, which showed the lowest cooling temperature of the data set.

References

[1]Spanjers, G. G., Bromaghim, D. R., Lake, Capt. J., Dulligan, M., White, D., Schilling, J. H., Bushman, S. S., Antonsen, E. L., Burton, R. L., Keidar, M., and Boyd, I. D., "AFRL Micro-PPT Development for Small Spacecraft Propulsion," AIAA Paper 2002-3974, July 2002.

[2]Spanjers, G. G., Lotspeich, J. S., McFall, K. A., and Spores, R. A., "Propellant Losses Because of Particulate Emission in a Pulsed Plasma Thruster," *Journal of Propulsion and Power*, Vol. 14, No. 4, 1998, pp. 554–559.

[3]Burton, R. L., Rysanek, F., Antonsen, E. L., Wilson, M. J., and Bushman, S. S., "Pulsed Plasma Thruster Performance for Microspacecraft Propulsion," Micropropulsion for Small Spacecraft, edited by M. Micci, Progress Series, AIAA, Reston, VA, 2000, Chap. 13.

[4]Antonsen, E. L., Burton, R. L., Spanjers, G. G., and Engelman, S. F., "Herriott Cell Augmentation of a Quadrature Heterodyne Interferometer," *Review of Scientific Instruments*, Vol. 74, No. 1, 2003, pp. 88–93.

[5]Spanjers, G. G., Malak, J. B., Leiweke, R. J., and Spores, R. A., "The Effect of Propellant Temperature on Efficiency in a Pulsed Plasma Thruster," *Journal of Propulsion and Power*, Vol. 14, No. 4, 1998, pp. 545–553.

[6]Zehnder, A. T., and Rosakis, A. J., "On the Temperature Distribution at the Vicinity of Dynamically Propagating Cracks in 4340 Steel: Experimental Measurements Using High-Speed Infrared Detectors," *Journal of the Mechanics and Physics of Solids*, Vol. 39, No. 3, 1991, pp. 385–417.

[7]Mason, J. J., and Rosakis, A. J., "On the Dependence of the Dynamic Crack Tip Temperature Fields in Metals upon Crack Tip Velocity and Material Parameters," *Mechanics of Materials*, Vol. 16, No. 4, 1992, pp. 337–350.

[8]Antonsen, E. L., "Propellant Surface Temperature and Plume Characteristics of Micro-Pulsed Plasma Thrusters," Ph.D. Dissertation, Dept. of Aeronautical and Astronautical Engineering, Univ. of Illinois at Urbana–Champaign, May 2004.

[9]Keidar, M., and Boyd, I. D., "Optimization Issues for a Micro-Pulsed Plasma Thruster," AIAA Paper 2004-4119, July 2004.

[10]Keidar, M., Boyd, I. D., Antonsen, E. L., Gulczinski, F. S., III, and Spanjers, G. G., "Propellant Charring in Pulsed Plasma Thrusters," *Journal of Propulsion and Power*, Vol. 20, No. 6, 2004, pp. 978–984.

[11]Keidar, M., Boyd, I. D., Antonsen, E. L., and Spanjers, G. G., "Progress in Development of Modeling Capabilities for a Micro-Pulsed Plasma Thruster," AIAA Paper 2003-5166, July 2003.

[12]Burton, R. L., and Turchi, P. J., "Pulsed Plasma Thruster," *Journal of Propulsion and Power*, Vol. 14, No. 4, 1998, pp. 716–735.

[13]Wentink, T., Jr., "High Temperature Behavior of Teflon," Avco-Everett Research Lab. AFBMD-TN-59-15 Research Rep. 55, Everett, MA, July 1959.

[14]Madou, M. J., *Fundamentals of MicroFabrication: The Science of Miniaturization*, 2nd ed., CRC Press, Boca Raton, FL, 2002, Chap. 3.

[15]Anderson, J. D., Jr., *Modern Compressible Flow*, 2nd ed., McGraw–Hill, New York, 1990, Chap. 7.

[16]Jahn, R. G., *Physics of Electric Propulsion*, McGraw–Hill, New York, 1968, Chap. 9.